

1  
2  
3  
4  
5 Zonal propagation of near surface zonal currents in relation to surface wind forcing in  
6 the equatorial Indian Ocean  
7  
8  
9

10  
11 Motoki Nagura<sup>1</sup>  
12

13 <sup>1</sup> Japan Agency for Marine-Earth Science and Technology, Yokosuka, Kanagawa, Japan  
14

15  
16 Michael J. McPhaden<sup>2</sup>  
17

18 <sup>2</sup> NOAA/Pacific Marine Environmental Laboratory, Seattle, Washington  
19  
20  
21  
22  
23  
24  
25  
26  
27  
28  
29

30 <sup>1</sup> *Corresponding author address:* 2-15 Natsushima-cho, Yokosuka, Kanagawa,  
31 237-0061

32 *E-mail:* nagura@jamstec.go.jp  
33

## ABSTRACT

Zonal propagation of zonal velocity along the equator in the Indian Ocean and its relationship with wind forcing are investigated with a focus on seasonal time scales using in-situ observations from four acoustic Doppler current profilers (ADCPs) and an ocean reanalysis dataset. Our results show that the zonal phase speed of zonal currents varies depending on season and depth in a very complicated way in relation to surface wind forcing. Surface layer zonal velocity propagates to the west in northern spring but to the east in fall in response to zonally propagating surface zonal winds, while in the pycnocline zonal phase speed is related to wind forced ocean wave dynamics. In the western half of our analysis domain ( $78^{\circ}$ - $83^{\circ}$ E), zonal phase speed in the pycnocline is eastward all year, which we attribute to the radiation of Kelvin waves forced in the western basin. In the eastern half of our domain ( $80^{\circ}$ - $90^{\circ}$ E), zonal phase speed is westward at 50- to 100-m depths in northern fall, but eastward above and below, most likely due to Rossby waves generated at the eastern boundary.

56

## 57 1. Introduction

58 In the equatorial Pacific and Atlantic Oceans, the westward flowing South  
59 Equatorial Current (SEC) at the surface and eastward flowing Equatorial Undercurrent  
60 (EUC) in the thermocline are permanent features of the ocean circulation (e.g., Wyrтки  
61 and Kilonsky 1984; Stramma and Schott 1999; Yu and McPhaden 1999; Johnson et al.  
62 2002; Johns et al. 2014). They are driven by the easterly trade winds (e.g., Philander  
63 and Pacanowski 1980), with seasonal variability dominated by annual, or in the case of  
64 surface currents in the Atlantic Ocean, semiannual variability (Yu and McPhaden 1999;  
65 Richardson and McKee 1984; Brandt et al. 2014).

66 In the Indian Ocean, the surface winds change direction seasonally in relation to the  
67 monsoons, and currents in and above the thermocline are transient. Zonal velocity near  
68 the surface in the equatorial Indian Ocean, referred to as the Wyrтки jet after Wyrтки  
69 (1973), is eastward twice per year in northern spring and fall. Subsurface zonal currents  
70 in the Indian Ocean are eastward only in early northern spring and fall and westward in  
71 the rest of the year (Knauss and Taft 1964; Knox 1976; Reppin et al. 1999; Iskandar et  
72 al. 2009; Nyadjro and McPhaden 2014).

73 Previous studies pointed out that seasonal variability in equatorial zonal currents is  
74 largely governed by wind-driven linear wave dynamics in all the three basins (Yu and  
75 McPhaden 1999; Ding et al. 2009; Nagura and McPhaden 2010; Nagura and McPhaden  
76 2014). On seasonal time scales, the available large scale  $O(1000 \text{ km})$  zonal wavelength)  
77 wave modes are the non-dispersive Kelvin wave and long Rossby waves.

Observations indicate that the SEC and EUC in the Pacific (Yu and McPhaden 1999), the SEC in the Atlantic (Richardson and McKee 1984; Ding et al. 2009) propagate to the west under the dominant influence of Rossby wave dynamics.

In this study, we examine zonal phase propagation of zonal velocity and its phase relationship with zonal wind forcing on seasonal time scales along the equator in the Indian Ocean. Previous studies suggested that the Wyrтки jets in the Indian Ocean propagated to the west in response to surface wind forcing (Molinari et al. 1990; Qiu et al. 2009; Nagura and McPhaden 2010). Both wind-driven and boundary-generated Rossby waves contribute to the Wyrтки jets (e.g., Han et al. 1999; Yuan and Han 2006; Nagura and McPhaden 2010). We now have multi-year long moored acoustic Doppler current profiler (ADCP) records at four locations along the equator to update and refine these results (Fig.1a). The ADCPs were deployed where surface winds are affected by the seasonal migration of atmospheric deep convection in the eastern half of the basin, which leads to a complicated pattern of surface wind forcing.

We also examine zonal phase propagation in subsurface zonal velocity, focusing on the transient undercurrents in the Indian Ocean, which have not been fully investigated. Sengupta et al. (2007), Iskandar et al. (2009) and Chen et al. (2015) pointed out that seasonal variability in the Indian Ocean EUCs is attributable to wind-forced waves and boundary generated equatorial waves. In particular, Chen et al. (2015) showed that wind-forced Kelvin and Rossby waves are mainly responsible for variability observed in the western basin, whereas boundary generated Rossby waves are important in the eastern basin. However, Chen et al. (2015) used numerical models

(an ocean general circulation model, OGCM, and a linear model) and adopted an artificial damper near the eastern boundary to separate wind-driven variability from boundary generated Rossby waves, while Sengupta et al. (2007) conducted idealized experiments using an OGCM. Iskandar et al. (2009) examined the wave propagation tendencies in satellite altimetry but only qualitatively related these tendencies to observed variations in zonal current velocity. We quantitatively estimate zonal phase speed using in-situ observations, which complements both previous empirical work of Iskandar et al. (2009) and the numerical experiments of Sengupta et al. (2007) and Chen et al. (2015). As a guide to interpreting our kinematic analysis of in-situ observations, we perform a complementary dynamical analysis based on WKB theory. Luyten and Roemmich (1982) applied this theory to semiannual variability in zonal velocity below the pycnocline (200- to 750-m depths) in the equatorial Indian Ocean. Here we use it to diagnose currents in and above the pycnocline.

The rest of the paper is organized as follows. The data we use are described in section 2. We use an ocean reanalysis dataset in addition to ADCP observations. Obtained results are described in section 3, and dynamical interpretation is presented in section 4. The main results are summarized in the last section. We use northern seasons below.

## 2. Data

We use the daily averages of zonal velocity obtained from upward-looking ADCPs moored at  $78^{\circ}$ ,  $80.5^{\circ}$ ,  $83^{\circ}$  and  $90^{\circ}$ E on the equator, which were collected as a part of the

Research Moored Array for African-Asian-Australian Monsoon Analysis and Prediction (McPhaden et al. 2009). Locations of ADCP moorings are shown in Fig.1a. The ADCPs are mounted in floats with the target depths of 300 m. In this study we use records at depths shallower than 250 m, but discarded velocity retrievals in the upper 30 m because they are contaminated by backscatter from the ocean surface. We replaced the surface data with the values extrapolated from the shallowest depths where good data were available. This extrapolation provides a reasonable estimate based on the high correlation between zonal velocity at the surface and below (Nagura and McPhaden 2010; McPhaden et al. 2015; Wang et al. 2015). Observations are gridded at the 5-m intervals at 78°, 80.5° and 83°E and the 10-m intervals at 90°E. We interpolated data at 90°E into the 5-m intervals for the consistency with the other locations. The time series of records at 78°, 80.5° and 83°E on the equator had long data gaps due to instrument or mooring failure (from 20 November 2009 to 19 December 2010 at 78°E, from 18 October 2008 to 1 September 2009 at 80.5°E and from 12 December 2010 to 26 July 2011 at 83°E). These gaps were filled by linear regression (Wang et al. 2015), in which regression coefficients were first calculated using available data between the target mooring site and the nearest neighboring sites at each depth. Then, data gaps at the target location were filled using the regression relationship, providing that data were available at the neighboring sites. The time history of the filled time series is shown in Fig.1b. No interpolation was made for time series at 90°E since there were no neighboring ADCP moorings for this site.

In addition to velocity data, we examine temperature and salinity data compiled by

Roemmich and Gilson (2009). After an initial quality check, Argo float observations are linearly interpolated in the vertical direction and mapped onto a  $1^\circ \times 1^\circ$  grid based on a least squares fit and an objective analysis. The period of this dataset is from January 2004 to October 2014.

For comparison with ADCP observations, we use the ocean reanalysis dataset obtained from European Centre for Medium-Range Weather Forecasts (ECMWF) Ocean Reanalysis System 4 (ORA-S4; Balmaseda et al. 2013). The ORA-S4 product is constructed by assimilating various observations into version 3.0 of the Nucleus for European Modeling of the Ocean model (Madec 2008) with a variational assimilation method. Assimilated data include temperature and salinity profiles obtained from expendable bathythermographs, conductivity-temperature-depth sensors, mooring buoys and autonomous pinniped bathythermograph and satellite altimetry data. No assimilation was made for velocity. The model is forced by surface momentum, heat and freshwater fluxes obtained from the atmospheric ECMWF reanalysis (ERA; Uppala et al. 2005; Dee et al. 2011). Horizontal grid intervals are  $1^\circ$  in the zonal direction and  $0.3$  to  $1.0^\circ$  in the meridional direction with the minimum meridional grid interval on the equator. The model has 42 vertical levels. The first 18 levels correspond to the upper 200 m. ORA-S4 output is provided as monthly averages.

We calculate surface wind stress using daily averages of surface wind data of the ERA Interim reanalysis (Dee et al. 2011). Output from the ERA reanalysis is on a  $1.5^\circ \times 1.5^\circ$  grid and available for the period from 1 January 1989 to 31 December 2014. A standard bulk formula is used for wind stress calculation with a drag coefficient of 1.43

166  $\times 10^{-3}$  and air density of  $1.225 \text{ kg m}^{-3}$ .

### 168 3. Kinematic Description

#### 169 a. Time series

170 To focus on seasonal variability, we calculate mean seasonal cycles of zonal  
171 velocity for the period from 2005 to 2013, in which ADCP observations are available at  
172 more than two locations along the equator (Fig.1b). We computed mean seasonal cycles  
173 for ADCP observations based on record length means at each location. This may lead to  
174 some inconsistencies, as the period of ADCP records is different from place to place.  
175 For example, the time series at  $0^\circ, 78^\circ\text{E}$  includes a negative Indian Ocean dipole (IOD)  
176 event in 2010 and a positive IOD event in 2012, whereas that at  $0^\circ, 80.5^\circ\text{E}$  includes two  
177 positive events (2006 and 2012) and one negative event (2010; Fig.1c). Thus, we also  
178 compute seasonal cycles using the ocean reanalysis, sampling velocity time series  
179 obtained from ORA-S4 for the same period and location as the ADCP moorings. In  
180 addition we calculate the mean seasonal cycles using the full time series of reanalysis  
181 velocity and compare two results.

182 Figure 2a shows mean seasonal cycles for observed zonal velocity at  $0^\circ, 78^\circ\text{E}$ .  
183 Currents near the surface are eastward in April-May and September-December, which  
184 are the Wyrtki jets. The fall Wyrtki jet is swifter and deeper compared to the spring  
185 counterpart. Eastward zonal velocity shows a separated EUC core at about 100-m depth  
186 in March-April and extends to the levels deeper than the 200-m depth. The fall eastward  
187 EUC is observed in August-September in the pycnocline, but with a much weaker

amplitude and shallower bottom depth compared to the spring EUC. Zonal velocity at 80.5°E (Fig.2b) and 83°E (Fig.3a) is similar to that at 78°E in terms of the dominance of semiannual variability and a separated eastward EUC core in boreal spring. Zonal velocity at 90°E shows a different pattern on the other hand (Fig.3b). In March and April, velocity at 90°E tends to be eastward in the upper 200 m with cores near the surface and at about 120-m depth. In June and July currents are eastward from the surface through about 100-m depth. An eastward current appears in September with its core at about 70-m depth. This eastward flow lasts until late November, with maximum flow shoaling from about 70-m in September to about 50-m in late November. Currents in the upper 30 m depth are westward from July to October and eastward from November to January. These patterns are clearly different from those at 78°-83°E. At all the locations, zonal currents at deeper levels lead those at shallower levels at and below the pycnocline, i.e., vertical phase speed is upward below the surface.

The middle panels in Figs. 2 and 3 show mean seasonal cycles calculated from reanalysis velocity time series sampled in the same manner as ADCP observations. Results compare well with those obtained from ADCP observations in terms of a stronger eastward current near the surface in fall than in spring at 78°, 80.5° and 83°E, a stronger eastward current in the pycnocline in spring than in fall at the same locations, and the presence of an eastward subsurface current in the upper pycnocline at 90°E in fall. This good comparison indicates that the reanalysis dataset reproduces observed variability reasonably well. However, there is noticeable discrepancy in the magnitude of the spring eastward EUC compared to observations, with the reanalysis tending to

underestimate the magnitude of this flow. The underestimate of subsurface velocity variability is also confirmed by wavelet analysis as described below. The reasons for this underestimation of velocity power are unknown. Possible explanations include the sensitivity of reanalysis currents to the parameterization of vertical mixing in the ORA-S4 model (though Balmaseda et al. (2013) did not mention which scheme is used) and inaccuracies in the wind forcing. In addition to zonal velocity magnitude, the reanalysis shows a minor discrepancy in the zonal phase speed of upper pycnocline currents in fall and winter, which will be discussed in more detail below.

Mean seasonal cycles obtained from the full reanalysis time series over the period 2005-2013 are shown in the bottom panels of Figs. 2 and 3. The differences between mean seasonal cycles obtained from the full record length vs subsampled reanalysis time series are minor, with patterns of seasonal current variability described in the observations also found in the results obtained from the full reanalysis time series. These results indicate that the time history of ADCP sampling is long enough to estimate reliable mean seasonal cycles.

Zonal phase propagation of zonal velocity can be examined in longitude-time diagrams (Fig.4). Observed surface zonal velocity (Fig.4a) shows the westward propagation of an eastward current in March-May. In fall, velocity increases from July to late November at 78°E, while it increases from early October to mid-December at 90°E, showing a tendency of eastward phase propagation. At 80-m depth, which is located in the upper pycnocline, eastward velocity peaks in early April at 78°E and in mid-May at 90°E (Fig.4b), indicating eastward phase speed. In fall, eastward velocity

at 80-m depth propagates to the west from 90° to 83°E in September-December but it propagates to the east from 78° to 83°E in October-December. Zonal velocity at 120-m depth, which is in the lower pycnocline, shows a slight tendency of eastward phase propagation in particular in spring (Fig.4c), as indicated by the reversal of zonal velocity from eastward to westward in mid-May at 78°E and in late May at 90°E.

The middle panels in Fig.4 show zonal velocity mean seasonal cycles obtained from ORA- S4 time series that are sampled at the same time and locations as ADCP observations. Westward phase propagation in spring and eastward propagation in fall are seen in surface velocity (Fig.4d). Velocity at 80-m depth shows eastward phase propagation in spring and westward propagation in fall in a consistent manner with observations, but eastward phase propagation is not seen in the reanalysis results in the western half of the domain in October-December (Fig.4e). The tendency of eastward phase propagation is observed at 120-m depth from July to November, in particular in the eastern part of the domain (Fig.4f). These characteristics compare well with those from the observations. Results obtained from the full 2005-2013 time series of reanalysis velocity (Fig.4g-i) also compare well with those from observations and from the subsampled reanalysis time series, which indicate that zonal phase propagation detected in observations is not sensitive to the relatively short record lengths.

We repeated the same computation of mean seasonal cycles for the period from 1958 to 2014 using the reanalysis and found that propagation tendencies were similar (figure not shown). Thus, propagation tendencies shown here are representative of long-term characteristics. Also, we examined propagation tendencies in zonal velocity

on isopycnals by interpolating ADCP zonal velocity onto isopycnals calculated from observed temperature and salinity. Results were similar to those at 80- and 120-m depths shown in the middle and right panels in Fig. 4. Thus, the zonal gradient of the pycnocline depth does not fundamentally affect our conclusions.

#### b. Wavelet analysis

The direction of phase propagation in zonal velocity varies seasonally (Fig.4) so in this section, we quantitatively estimate zonal phase speed by applying wavelet analysis to examine this temporal modulation. We obtained the essentially same results if we used complex demodulation analysis (Kessler et al. 1995), which also takes temporal modulation into account. Mean seasonal cycles of zonal velocity are used in the analysis, though we later look at variability year by year. We use the Paul wavelet function, which is advantageous in examining a temporally localized signals (Torrence and Compo 1998). In the rest of this section, mean seasonal cycles for reanalysis velocity are computed from the full (2005-2013) time series. We do not show results obtained from the reanalysis time series that is sampled in the same manner as ADCP observations, since they are essentially identical.

Temporally averaged wavelet power for observed zonal velocity shows the dominance of semiannual variability from the surface to the pycnocline (Fig.5a-d). At 78°E, semiannual power is largest in the upper 30 m and decreases with depth. At 80.5° and 83°E, a local peak of semiannual power is found in the pycnocline in addition to the surface peak. At 90°E, the maximum of semiannual power is located at 120-m depth.

Wavelet power for reanalysis velocity peaks at the semiannual period as well (Fig.5e-h) though the reanalysis tends to overestimate semiannual power near the surface compared to the observations. The subsurface peak in semiannual power is also reproduced in the reanalysis at 83° and 90°E, although power is underestimated there, which represents a weaker EUC in the reanalysis compared to observations (Figs. 2 and 3).

Considering the dominance of semiannual variability, we calculated zonal phase speed of zonal velocity using wavelet phase at a period of 180-days. It is evident that zonal phase speed for zonal velocity can be different between the eastern and western parts of the domain (Figs.4b), so we calculate phase speed between 78°-83°E and 80.5°-90°E separately. If semiannual power is below the 95% confidence level, the corresponding phase is excluded from the phase speed calculation. The 95% level for wavelet power is calculated following Torrence and Compo (1998).

Phase speed is defined as follows. For an arbitrary variable  $X = X_0 e^{i\varphi}$ , where  $X_0$  is amplitude and  $\varphi$  is phase, frequency ( $\sigma$ ) and zonal wavenumber ( $k$ ) are defined as  $\sigma = -\partial_t \varphi$  and  $k = \partial_x \varphi$ , respectively. The Taylor expansion yields  $\varphi = -\sigma t + kx$ , if we ignore the second and higher order terms, where  $x$  and  $t$  are longitude and time, respectively. A line of constant phase is defined as  $-\sigma t + kx = \text{constant}$ . Differentiating this equation with respect to  $t$ , we obtain zonal phase speed,  $dx/dt = \sigma/k$ . In our definition, positive phase speed indicates eastward propagation, and negative means westward. In our case  $\sigma = -2\pi/(180 \text{ days})$ , and  $k$  is calculated as  $k = \Delta\varphi/\Delta x$ , where  $\Delta\varphi$  is zonal phase difference between two locations, and  $\Delta x$  is

their zonal distance. Note that phase speed becomes very large between the regions of eastward and westward phase propagation, where a pattern is nearly stationary, and  $\Delta\varphi$  and  $k$  are close to zero.

Zonal phase speed between  $78^\circ$  and  $83^\circ\text{E}$  shows a different seasonal variability between the near surface and the pycnocline (Fig.6a). In the upper 50 m, zonal phase speed is eastward from September to March and westward from May to July, which represents the seasonal modulation of propagation direction in surface velocity shown in Fig.4a. At 90- to 140-m depths, phase speed is eastward all year reflecting the prevalence of eastward phase speed in the western part of the domain shown in Figs. 4b and 4c.

Phase speed between  $80.5^\circ$  and  $90^\circ\text{E}$  (Fig.6b) is westward and eastward near the surface in February-May and July-January, respectively, which is similar to but leads by a few months surface phase speed between  $78^\circ$  and  $83^\circ\text{E}$ . At 50- to 100-m depths, phase speed is eastward from May to July but westward from September to January. The westward phase speed in fall is also seen in the longitude-time diagram for velocity at 80-m depth (Fig.4b) and can be related to the eastward subsurface current at  $90^\circ\text{E}$  in September-December (Fig.3b). Phase speed between  $80.5^\circ$  and  $90^\circ\text{E}$  is eastward all year in the 100- to 130-m depth range.

Zonal phase speed is also calculated by applying wavelet analysis to mean seasonal cycles of reanalysis zonal velocity. Reanalysis velocity phase speed between  $78^\circ$  and  $83^\circ\text{E}$  changes sign in the upper 40 m seasonally, and it is mostly eastward all year at 80- to 140-m depths (Fig.7a). Between  $80.5^\circ$  and  $90^\circ\text{E}$ , phase speed is westward near the

surface and eastward in the pycnocline in March-April, whereas it reverses from eastward to westward to eastward again from the surface to about 140-m depth in August-November (Fig.7b). These patterns compare well with those from observations (Fig.6). A discrepancy is found in phase speed between 78° and 83°E at 30- to 80-m depths in September-January, where observations show eastward phase speed (Fig.6a) but reanalysis results show westward phase speed (Fig.7a). This corresponds to the lack of eastward phase propagation in reanalysis zonal velocity in fall in the western half of the domain (Figs. 4e and 4h). Also, phase speed for observed zonal velocity between 80.5°E and 90°E is eastward all year at 100- to 130-m depths (Fig.6b), but reanalysis velocity phase speed is westward at these depths in December and January (Fig.7b). Vertical resolution of the reanalysis (~ 10 m) may not be high enough to reproduce eastward phase speed confined to the 30-m thick layer.

Using reanalysis output, we calculate zonal phase speed every 1° along the equator, using 10° intervals for the phase speed calculation ( $\pm 5^\circ$  around the central grid). Essentially the same results are obtained using zonal intervals from 1° to 20°. Surface phase speed for reanalysis velocity changes sign seasonally only across 75°-90°E (Fig.8a). Surface phase speed is mostly westward west of 75°E, which is consistent with the estimate of Nagura and McPhaden (2010). Phase speed at 80-m depth is eastward most of the time from about 70°E to 78°E but changes sign seasonally between 80°-90°E (Fig.8b). These patterns correspond to eastward phase speed below the surface between 78°-83°E (Fig. 6a) and seasonal reversal of subsurface phase speed in 80.5°-90°E (Figs. 6b and 7b), respectively. Also, the phase speed at 120-m depth tends

to be eastward for most of the time between 75° and 90°E (Fig.8c). Subsurface phase speed outside of these longitudes shows a completely different seasonal variability, which indicates that the characteristics detected by ADCPs are representative only of the region where the measurements were made.

In the above discussion, we calculated mean seasonal cycles first and then estimated zonal phase speed. Another method to examine climatological phase speed is to compute phase speed first for each year and then look for patterns that repeat every year. Results of this calculation for the ADCP observations show that surface phase speed between 78° and 83°E (Fig.9a) tends to be westward in April-June. Interannual variability is large in fall, but eastward phase speed is seen in some years from July to January. Phase speed between 78° and 83°E is mostly eastward at 80- and 120-m depths (Fig.9b,c). Between 80.5° and 90°E, phase speed tends to be westward in spring and eastward in fall near the surface (Fig.9d). Phase speed at 80-m depth between 80.5° and 90°E tends to be eastward in spring and westward in fall (Fig.9e), while at 120-m depth, it tends to be eastward all year (Fig.9f). These results indicate that the patterns of zonal phase speed obtained from mean seasonal cycles are found in respective years.

#### 4. Dynamical Interpretation in terms of WKB theory

Previous studies showed that surface and subsurface zonal currents in the equatorial Indian Ocean are driven by the surface zonal winds along the equator (e.g., Nagura and McPhaden 2010; Chen et al. 2015). Climatological zonal wind stress in the equatorial Indian Ocean is eastward twice a year in boreal spring and fall east of 50°E (Fig.10a).

The westerly winds are stronger in the fall than in the spring, which is probably why the Wyrтки jet is stronger in fall than in spring (e.g., Fig.2a). From 80° to 95°E, westerly winds tend to migrate to the west from March to May but to the east from October to January. These propagation tendencies can be confirmed by zonal phase speed at 180-day periods estimated with wavelet analysis (Fig.10b). These zonal migrations of zonal wind stress are related to the movement of atmospheric deep convection. In spring, atmospheric deep convection moves northwestward from the Maritime Continent to the northern Bay of Bengal during the transition from the Australian to Indian monsoons (Webster et al. 1998). As westerly wind near the surface flows into the convective center (e.g., Gill 1980), westerlies migrate to the west along the equator, following the movement of atmospheric convection (Fig.11). In fall, atmospheric convection moves southeastward, and westerlies migrate to the east along the equator.

The direction of zonal wind stress phase propagation agrees well with that of surface zonal velocity phase speed (Figs. 6, 7, 8a and 10b). This coincidence suggests that seasonal reversal of surface velocity phase speed is caused by the wind pattern. The only discrepancy between wind and surface velocity phase speeds is found from June to October, in which surface velocity phase speed is eastward, but wind phase speed is westward. In this season, westerly wind is confined to the region west of 90°E (Fig.10a). The linear model results of Nagura and McPhaden (2010) show that Kelvin waves radiate to the east from this wind patch (their Fig.10b), which is a likely explanation for summertime eastward phase speed of surface zonal velocity.

Zonal phase speed in the pycnocline is eastward all year between 78° and 83°E

(Fig.6a and 7a) consistent with the prominence of equatorial Kelvin waves at these longitudes. To examine the role of these wave dynamics more quantitatively, we estimated the propagation path of wave energy based on ray tracing techniques (e.g., Bühler 2014). This diagnostic tool, based on the wave dispersion relation, has the advantage that it does not require numerical integration of the basic equations. Caveats are that the method deals with refraction of waves but not their reflection, and that it fails at caustics where waves break and are absorbed by the mean current. To examine the full wave dynamics, a numerical model is necessary, such as multi-vertical mode linear wave models used by Rothstein et al. (1985), McPhaden et al. (1986) and Nagura and McPhaden (2010) or a more sophisticated general circulation model.

The dispersion relation of vertically propagating waves depends on stratification. To consider refraction of waves due to spatial changes in stratification, we apply the WKB approximation (e.g., McCreary 1984), which assumes that waves are embedded in a spatially varying background state, and that the wavelength is significantly shorter than the scale of the background state variation (e.g., Bühler 2014). This scale separation allows one to calculate wave trajectories that slowly vary in relation to background state. The accuracy of this approximation is measured by the parameter  $m^{-2}\lambda_z^{-2}$ , where  $m$  is vertical wavenumber of waves,  $\lambda_z = N^{-1}\partial_z N$  is the vertical scale for background stratification and  $N$  is Brunt-Väisälä frequency. If this parameter is significantly less than unity, the approximation holds. We estimated  $m$  from mean seasonal cycles of ADCP zonal velocity by fitting a straight line to its wavelet phase at the semiannual period from 50- to 150-m depths.  $N$  is calculated from potential density obtained from

Roemmich and Gilson's (2009) dataset as the average over the period from 2005 to 2013 and from 3°S to 3°N. The resulting  $m^{-2}\lambda_z^{-2}$  averaged over 50- to 150-m depths along the equator in the Indian Ocean is about 0.35, indicating the validity of the WKB approximation for our problem. The dispersion relations for the Kelvin and first meridional mode long Rossby waves are  $\sigma = Nk/m$  and  $\sigma = -Nk/(3m)$ , respectively.

Ray trajectories of semiannual Kelvin waves are directed downward to the east (Fig.12b) so that Kelvin waves excited at the surface in the western basin reach pycnocline depth in the eastern basin. The amplitude of semiannual variability in zonal wind stress is larger in the western and central parts of the basin than in the eastern basin (Fig.12a), which is the likely energy source for the Kelvin waves. Zonal velocity in the pycnocline tends to propagate upward (Figs.2 and 3 in this study; McPhaden 1982; Nyadjro and McPhaden 2014), which indicates downward energy propagation for equatorial waves (McCreary 1984), consistent with an energy source at the surface.

Between 80.5° and 90°E, zonal phase speed at 50- to 100-m depths is westward only in fall and winter, sandwiched between eastward phase speed near the surface and at 100- to 130-m depths (Figs.6b and 7b). Eastward phase speed at 100- to 130-m depths is most likely due to Kelvin waves as is discussed above. Conversely, the subsurface westward phase speed is most likely due to Rossby wave dynamics, with semiannual Rossby waves generated at the eastern boundary reaching pycnocline depths between 80°-90°E (Fig.12c). In fall and winter, both surface zonal wind and surface zonal velocity propagate to the east in 80°-90°E (Figs. 6b, 7b and 10b), indicating the

prominence of Kelvin waves. Wind-driven surface Kelvin waves hit the eastern boundary and are reflected back into the interior as boundary generated Rossby waves, which would lead to westward phase speed below the surface. However, semiannual Rossby waves radiated from the eastern boundary reach 100-m depths or below at the ADCP locations (Fig.12c), which is deeper than the depths of westward phase speed (50- to 100-m depths; Figs. 6b and 7b). A possible cause for this discrepancy is discussed in the last section.

Using  $N$  and  $m$  estimated above, phase speeds can be calculated based on the dispersion relation. Results indicate a phase speed of  $0.97 \text{ m s}^{-1}$  for the Kelvin wave and  $0.32 \text{ m s}^{-1}$  for the first meridional mode Rossby wave. The typical eastward phase speeds at 100-m depth estimated from ADCP observations are  $0.8$  to  $1.2 \text{ m s}^{-1}$  (Fig. 6), which roughly coincides with Kelvin wave phase speed expected from the dispersion relation. Westward phase speed at about 75-m depth in fall and winter is about  $-0.75 \text{ m s}^{-1}$  (Fig. 6b), which is considerably faster than the theoretical estimate of Rossby wave phase speed. This discrepancy is discussed below in the final section.

## 5. Summary and Discussion

We examine zonal phase speed of zonal velocity and its phase relationship with surface wind forcing in the eastern equatorial Indian Ocean using in-situ velocity observations obtained from four ADCPs along the equator ( $78^\circ$ ,  $80.5^\circ$ ,  $83^\circ$  and  $90^\circ\text{E}$ ) and the ORA-S4 reanalysis dataset. We focus on seasonal variability in zonal velocity from the surface to the upper pycnocline where ADCP observations are available. We

calculate mean seasonal cycles based on the full record of ADCP observations at each location for the period from 2005 to 2013. The period of the observational records is different from location to location, which could lead to uncertainties in our results. To estimate this uncertainty, we sample reanalysis velocities at the same locations and times as ADCP observations and then calculate mean seasonal cycles. Results compare well with mean seasonal cycles obtained from the full time series of reanalysis velocity, which indicates that the results presented here are not overly sensitive to the details of data sampling. We also find that in-situ observations and reanalysis output give consistent results.

We investigate zonal phase propagation of zonal currents using longitude-time diagrams and wavelet analysis. Results reveal that the spring Wyrtki jet tends to propagate to the west at the ADCP locations (from  $78^{\circ}$  to  $90^{\circ}$ E), whereas the fall Wyrtki jet propagates to the east. We found that zonal wind propagates in the same direction as surface zonal velocity. In spring, atmospheric deep convection moves northwestward during the transition from the Australian to Indian monsoons, and wind moves to the west along the equator. Atmospheric convection and zonal wind move in the opposite direction in fall. The seasonal modulation of propagation direction in surface zonal velocity is thus only seen in the eastern Indian Ocean.

In the western part of our analysis domain ( $78^{\circ}$ - $83^{\circ}$ E), phase speed in the pycnocline is eastward all year. Ray trajectories calculated based on the WKB approximation show that semiannual Kelvin waves excited at the surface in the western basin reach pycnocline depth in the eastern basin, resulting subsurface eastward phase speed there.

Semiannual variability in zonal wind is more energetic in the western half of the basin than in the east, which is a likely energy source for these Kelvin waves.

In fall, both surface zonal wind and surface zonal velocity propagate to the east. However phase speed between  $80.5^{\circ}$ - $90^{\circ}$ E is westward in the upper pycnocline (50- to 100-m depths) in fall, possibly due to boundary generated Rossby waves. When wind-driven Kelvin waves hit the eastern boundary, they generate Rossby waves that propagate downward to the west, giving rise to westward phase speeds below the surface. As a result, zonal phase speed in fall shows a complicated vertical structure between  $80.5^{\circ}$ - $90^{\circ}$ E, i.e., eastward in the upper 50 m owing to propagating surface wind forcing, westward at 50- to 100-m depths which is possibly caused by Rossby wave dynamics, and eastward at 100- to 130-m depths due to Kelvin wave trajectories.

We obtained similar patterns of zonal phase speed with a different method, which includes the calculation of velocity mean seasonal cycles for a longer period, the analysis of velocity on isopycnals and the phase speed estimate with complex demodulation analysis. These results demonstrate the robustness of the detected patterns.

One uncertainty in our dynamical interpretation is the depths of westward phase speed in fall and winter between  $80.5^{\circ}$  and  $90^{\circ}$ E (Figs. 6b and 7b). The depths of westward phase speed (50- to 100-m depths) do not exactly coincide with Rossby wave trajectories emanating from the eastern boundary, which reach 100-m depth or below at ADCP locations (Fig.12c). Also, westward phase speeds estimated from observations are too fast compared to that calculated based on the dispersion relationship of the first

meridional mode Rossby wave. A possible cause of these discrepancies is that the pycnocline is sharp and thin near the eastern boundary (Figs.12b and 12c). We base our analysis on the WKB approximation, which can be invalid in the region where the background state varies rapidly. Also, a sharp pycnocline leads to the reflection of vertically propagating waves (Philander 1978), which is not considered by the calculation of ray trajectories. Numerical simulations are necessary to examine the exact wave propagation path, which is beyond the scope of our study.

Another uncertainty in our dynamical interpretation is the assumption of the dominance of linear dynamics. Seasonal variability in equatorial zonal velocity in the upper Indian Ocean is affected by nonlinear processes, such as momentum advection (e.g., Cane 1980; Nagura and McPhaden 2014) and mixed layer processes (e.g., Han et al. 1999). Also, Jensen et al. (2015) pointed out how intraseasonal wind bursts can contribute to the excitation of the Wyrтки jet. Although our analysis suggests the dynamics is predominantly linear, nonlinear processes may modify velocity phase speed, which is also beyond the scope of this study.

Regarding the comparison with results from previous studies, our results show the contributions from boundary generated Rossby waves and wind-driven Kelvin waves, which are consistent with results obtained by Sengupta et al. (2007), Iskandar et al. (2009) and Chen et al. (2015). Our results highlight detailed patterns of variability and suggest that the relative contributions from different wave modes vary seasonally, longitudinally, and vertically.

Our results exhibit a complicated vertical pattern of zonal phase speed, which has not

been pointed out before. This pattern is a unique feature of the Indian Ocean currents. The surface SEC propagates to the west in the Pacific (Yu and McPhaden 1999) and Atlantic Oceans (Ding et al. 2009). Similarly, the EUC propagates to the west in the Pacific (Yu and McPhaden 1999) while there is no clear indication of zonal propagation in the EUC of the Atlantic (Fig. 13 of Johns et al. 2014). One potential reason for the difference between the basins is the period of wind forcing, which is predominantly semiannual in the Indian Ocean but annual in the Pacific and Atlantic Oceans. At higher frequency, waves propagate more vertically so that higher vertical modes contribute more. Another possible factor is vertical viscosity. In the equatorial Pacific and Atlantic, the EUC and its vertical shear potentially damp high baroclinic modes via a strengthened vertical mixing due to dynamical instability (Rothstein et al. 1985; Wang and Müller 2002; Holmes and Thomas 2015) and/or the absorption of waves by the mean current (McPhaden et al. 1986; McPhaden and Ripa 1990). The absence of strong mean vertical shear of zonal velocity in the Indian Ocean presumably allows high baroclinic waves to propagate vertically more freely.

The actual zonal phase speed depends not only on the dominant frequency and wave's damping but also on other factors such as the spatial pattern of wind forcing and the interference of excited waves. Previous studies pointed out that the Wyrtki jets tend to propagate to the west (Molinari et al. 1990; Qiu et al. 2009; Nagura and McPhaden 2010). Our results reveal that the direction of phase propagation varies seasonally in the eastern basin related to the seasonal movements of atmospheric convection, which has not been pointed out before, whereas westward propagation dominates in the central and

western parts of the basin.

As for wave interference, many previous studies pointed out that a basin mode resonance contributes to the generation of the Wyrski jets, in which wind-driven waves and boundary generated waves constructively interfere for the second baroclinic mode and generate a focal point in zonal velocity (Cane and Moore 1981; Clarke and Liu 1993; Jensen 1993; Han et al. 1999; Han et al. 2001; Han 2005; Yuan and Han 2006; Fu 2007). When waves propagate vertically, implying the presence of multiple baroclinic modes, foci shift zonally with depth (Gent et al. 1983). Our results suggest that this is likely to occur, which is an interesting topic for future research.

#### Acknowledgments.

We thank anonymous two reviewers for their helpful comments on an earlier version of this manuscript. Wavelet software was provided by C. Torrence and G. Compo, and is available at URL: <http://paos.colorado.edu/research/wavelets/>. This study is partly supported by MEXT/JSPS KAKENHI Grant Number 26800249. This is PMEL contribution 4514.

## References

- Balmaseda, M. A., K. Mogensen, and A. T. Weaver, 2013: Evaluation of the ECMWF ocean reanalysis system ORAS4. *Q. J. R. Meteorol. Soc.*, 139, 1132-1161.
- Brandt, P., A. Funk, A. Tantet, W. E. Johns, and J. Fischer, 2014: The Equatorial Undercurrent in the central Atlantic and its relation to tropical Atlantic variability. *Clim. Dyn.*, 43, 2985-2997.
- Bühler, O., 2014: *Waves and mean flows*. Cambridge University Press, 33-37, 73-80.
- Cane, M. A., and D. W. Moore, 1981: A note on low-frequency equatorial basin modes. *J. Phys. Oceanogr.*, 11, 1578-1584.
- Chen, G., W. Han, Y. Li, D. Wang, and M. J. McPhaden, 2015: Seasonal-to-interannual time-scale dynamics of the equatorial undercurrent in the Indian Ocean. *J. Phys. Oceanogr.*, 45, 1532-1553.
- Clarke, A. J., and X. Liu, 1993: Observations and dynamics of semiannual and annual sea levels near the eastern equatorial Indian Ocean boundary. *J. Phys. Oceanogr.*, 23, 386-399.
- Dee, D. P., S. M. Uppala, A. J. Simmons, P. Berrisford, and Coauthors, 2011: The ERA-Interim reanalysis: Configuration and performance of the data assimilation system. *Q. J. R. Meteorol. Soc.*, 137, 553-597, doi:10.1002/qj.828.
- Ding, H., N. S. Keenlyside, and M. Latif, 2009: Seasonal cycle in the upper equatorial Atlantic Ocean. *J. Geophys. Res.*, 114, C09016, doi:10.1029/2009JC005418.
- Fu, L., 2007: Intraseasonal variability of the equatorial Indian Ocean observed from sea surface height, wind and temperature data. *J. Phys. Oceanogr.*, 37, 188-202.
- Gent, P.R., K. O'Neill, and M.A. Cane, 1983: A model of the semiannual oscillation in the equatorial Indian Ocean. *J. Phys. Oceanogr.*, 13, 2148-2160.
- Gill, A. E., 1980: Some simple solutions for heat-induced tropical circulation. *Quart. J. R. Met. Soc.*, 106, 447-462.
- Han, W., J. P. McCreary, D. L. T. Anderson, and A. J. Mariano, 1999: Dynamics of the eastern surface jets in the equatorial Indian Ocean. *J. Phys. Oceanogr.*, 29, 2191-2209.
- Han, W., 2005: Origins and dynamics of the 90-day and 30-60-day variations in the equatorial Indian Ocean. *J. Phys. Oceanogr.*, 35, 708-728.

601 Han, W., J. P. McCreary, Y. Masumoto, J. Vialard, and B. Duncan, 2011: Basin  
602 resonances in the equatorial Indian ocean. *J. Phys. Oceanogr.*, 41, 1252-1270.

603 Holmes, R. M., and L. N. Thomas, 2015: The modulation of equatorial turbulence by  
604 tropical instability waves in a regional ocean model. *J. Phys. Oceanogr.*, 45,  
605 1155-1173.

606 Iskandar, I., Y. Masumoto, and K. Mizuno, 2009: Subsurface equatorial zonal current in  
607 the eastern Indian Ocean. *J. Geophys. Res.*, 114, C06005,  
608 doi:10.1029/2008JC005188.

609 Jensen, T. G., 1993: Equatorial variability and resonance in a wind-driven Indian Ocean  
610 model. *J. Geophys. Res.*, 98 (C12), 22,533-22,552.

611 Jensen, T. G., T. Shinoda, S. Chen, and M. Flatau, 2015: Ocean response to  
612 CINDY/DYNAMO MJOs in air-sea-coupled COAMPS. *J. Meteor. Soc. Japan*,  
613 93A, 157-178.

614 Johns, W. E., P. Brandt, B. Bourlés, A. Tantet, A. Papapostolou, and A. Houk, 2014:  
615 Zonal structure and seasonal variability of the Atlantic equatorial undercurrent.  
616 *Clim. Dyn.*, 43, 3047-3069.

617 Johnson, G. C., B. M. Sloyan, W. S. Kessler, and K. E. McTaggart, 2002: Direct  
618 measurements of upper ocean currents and water properties across the tropical  
619 Pacific during the 1990s. *Progr. Oceanogr.*, 53, 31-61.

620 Kessler, W. S., M. J. McPhaden, and K. M. Weickmann, 1995: Forcing of intraseasonal  
621 Kelvin waves in the equatorial Pacific. *J. Geophys. Res.*, 100 (C6), 10 613-10  
622 631.

623 Knauss, J. A., and B. A. Taft, 1964: Equatorial undercurrent of the Indian Ocean.  
624 *Science*, 143, 354-356.

625 Knox, R. A., 1976: On a long series of measurements of Indian Ocean equatorial  
626 currents near Addu Atoll. *Deep-Sea Res.*, 23, 211-221.

627 Liebmann, B., and C. Smith, 1996: Description of a complete (interpolated) outgoing  
628 longwave radiation dataset. *Bull. Amer. Meteorol. Soc.*, 77, 1275-1277.

629 Luyten, J.R., and D.H. Roemmich, 1982: Equatorial currents at semi-annual period in  
630 the Indian Ocean. *J. Phys. Oceanogr.*, 12, 406-413.

631 Madec, G., 2008: NEMO reference manual, ocean dynamics component: NEMO-OPA.  
632 preliminary version. Tech. Rep. 27, Inst. Pierre-Simon Laplace, Paris, France.  
633 Note du Pole de Model.

634 McCreary, J. P., Jr., 1984: Equatorial beams. *J. Mar. Res.*, 42, 395-430.

635 McPhaden, M. J., 1982: Variability in the central equatorial Indian Ocean. *J. Mar. Res.*,  
636 40, 157-176.

637 McPhaden, M.J., J.A. Proehl, and L.M. Rothstein, 1986: The interaction of equatorial  
638 Kelvin waves with realistically sheared zonal currents. *J. Phys. Oceanogr.*, 16,  
639 1499–1516.

640 McPhaden, M. J., and P. Ripa, 1990: Wave-mean flow interactions in the equatorial  
641 ocean. *Annu. Rev. Fluid. Mech.*, 22, 167-205.

642 McPhaden, M. J., and Coauthors, 2009: RAMA: The Research Moored Array for  
643 African-Asian-Australian Monsoon Analysis and Prediction. *Bull. Amer.*  
644 *Meteorol. Soc.*, 90, 459-480.

645 McPhaden, M. J., Y. Wang, and M. Ravichandran, 2015: Volume transports of the  
646 Wyrtki jets and their relationship to the Indian Ocean dipole. *J. Geophys. Res.*  
647 *Oceans*, 120, doi:10.1002/2015JC010901.

648 Molinari, R. L., D. Olson, and G. Reverdin, 1990: Surface current distributions in the  
649 tropical Indian Ocean derived from compilations of surface buoy trajectories. *J.*  
650 *Geophys. Res.*, 95 (C5), 7217-7238, doi:10.1029/JC095iC05p07217.

651 Motell, C. E., and B. C. Weare, 1987: Estimating tropical Pacific rainfall using digital  
652 satellite data. *J. Clim. Appl. Meteor.*, 26, 1436-1446.

653 Nagura, M., and M. J. McPhaden, 2010: Wyrtki Jet dynamics: Seasonal variability. *J.*  
654 *Geophys. Res.*, 115, C07009, doi:10.1029/2009JC005922.

655 Nagura, M., and M. J. McPhaden, 2014: Zonal momentum budget along the equator in  
656 the Indian Ocean from a high-resolution ocean general circulation model. *J.*  
657 *Geophys. Res. Oceans.*, 119, 4444-4461, doi:10.1002/2014JC009895.

658 Nyadjro, E. S., and M. J. McPhaden, 2014: Variability of zonal currents in the eastern  
659 equatorial Indian Ocean on seasonal to interannual time scales. *J. Geophys. Res.*  
660 *Oceans.*, 119, 7969-7986, doi:10.1002/2014JC010380.

661 Philander, S. G. H., 1978: Forced oceanic waves. *Rev. Geophys. Space Phys.*, 16(1),  
662 15-46.

663 Philander, S. G. H., and R. C. Pacanowski, 1980: The generation of equatorial currents.  
664 *J. Geo- phys. Res.*, 85 (C2), 1123-1136.

665 Qiu, Y., L. Li, and W. Yu, 2009: Behavior of the Wyrtki Jet observed with surface  
666 drifting buoys and satellite altimeter. *Geophys. Res. Lett.*, 36, L18607,

doi:10.1029/2009GL039120.

Reppin, J., F. A. Schott, and J. Fischer, 1999: Equatorial currents and transports in the upper central Indian Ocean: Annual cycle and interannual variability. *J. Geophys. Res.*, 104, C7, 15 495-15 514.

Reynolds, R. W., N. A. Rayner, T. M. Smith, D. C. Stokes, and W. Wang, 2002: An improved in situ and satellite SST analysis for climate. *J. Clim.*, 15, 1609-1625.

Richardson, P. L., and T. K. McKee, 1984: Average seasonal variation of the Atlantic equatorial currents from historical ship drifts. *J. Phys. Oceanogr.*, 14, 1226-1238.

Roemmich, D., and J. Gilson, 2009: The 2004-2008 mean and annual cycle of temperature, salinity, and steric height in the global ocean from the Argo Program. *Prog. Oceanogr.*, 82, 81-100.

Rothstein, L. M., D. W. Moore, and J. P. McCreary, Jr., 1985: Interior reflections of a periodically forced equatorial Kelvin wave. *J. Phys. Oceanogr.*, 15, 985-996.

Saji, N. H., B. N. Goswami, P. N. Vinayachandran, and T. Yamagata, 1999: A dipole mode in the tropical Indian Ocean. *Nature*, 401, 360-363.

Sengupta, D., R. Senan, B. N. Goswami, and J. Vialard, 2007: Intraseasonal variability of equatorial Indian Ocean zonal currents. *J. Clim.*, 20, 3036-3055.

Stramma, L., and F. Schott, 1999: The mean flow field of the tropical Atlantic Ocean. *Deep-Sea Res.*, 46, 279-303.

Torrence, C., and G. P. Compo, 1998: A practical guide to wavelet analysis. *Bull. Amer. Meteor. Soc.*, 79 (1), 61-78.

Uppala, S. M., P. W. Kållberg, A. J. Simmons, U. Andrae, and Coauthors, 2005: The ERA-40 re-analysis. *Q. J. R. Meteorol. Soc.*, 131, 2961-3012.

Wang, D., and P. Müller, 2002: Effects of equatorial undercurrent shear on upper-ocean mixing and internal waves. *J. Phys. Oceanogr.*, 32, 1041-1057.

Wang, Y., M. J. McPhaden, P. Freitag, and C. Fey, 2015: Moored acoustic Doppler current profiler time series in the central equatorial Indian Ocean. NOAA Technical Memorandum, OAR- PMEL-146.

Webster, P. J., V. O. Magaña, T. N. Palmer, J. Shukla, R. A. Thomas, M. Yanai, and T. Yasunari, 1998: Monsoons: Processes predictability, and the prospects for prediction. *J. Geophys. Res.*, 103 (C7), 14 451-14 510.

Wyrtki, K., 1973: An equatorial jet in the Indian Ocean. *Science*, 181, 262-264.

Wyrtki, K., and B. Kilonsky, 1984: Mean water and current structure during the

Hawaii-to-Tahiti shuttle experiment. *J. Phys. Oceanogr.*, 14, 242-254.

Yu, X., and M. J. McPhaden, 1999: Seasonal variability in the equatorial Pacific. *J. Phys. Oceanogr.*, 29, 925-947.

Yuan, D., and W. Han, 2006: Roles of equatorial waves and western boundary reflection in the seasonal circulation of the equatorial Indian Ocean. *J. Phys. Oceanogr.*, 36, 930-944.

## LIST OF FIGURES

Fig. 1: (a) Locations of ADCP mooring sites ( $78^{\circ}\text{E}$ ,  $80.5^{\circ}\text{E}$ ,  $83^{\circ}\text{E}$  and  $90^{\circ}\text{E}$  along the equator;  $4^{\circ}\text{S}$ ,  $2.5^{\circ}\text{S}$ ,  $1.5^{\circ}\text{S}$ ,  $0.75^{\circ}\text{S}$ ,  $0^{\circ}$ ,  $0.75^{\circ}\text{N}$ ,  $1.5^{\circ}\text{N}$ , and  $2.5^{\circ}\text{N}$  along  $80.5^{\circ}\text{E}$ .

(b) Time history of ADCP sampling along the equator. The time series is from 9 August 2008 to 28 July 2013 at  $78^{\circ}\text{E}$ , from 27 October 2004 to 6 December 2013 at  $80.5^{\circ}\text{E}$ , from 8 August 2008 to 18 August 2014 at  $83^{\circ}\text{E}$ , and from 17 November 2000 to 5 June 2012 at  $90^{\circ}\text{E}$ . The data gap at  $90^{\circ}\text{E}$  is from 19 March 2009 to 10 November 2009.

(b) The index to the Indian Ocean dipole calculated from monthly averages of sea surface temperature (SST) obtained from the National Oceanic and Atmospheric Administration (NOAA) Optimum Interpolation (OI) SST dataset Version 2 (Reynolds et al. 2002). The Dipole mode index is defined as the difference in SST anomalies between the western Indian Ocean ( $10^{\circ}\text{S}$ - $10^{\circ}\text{N}$ ,  $50^{\circ}$ - $70^{\circ}\text{E}$ ) and the eastern equatorial Indian Ocean ( $10^{\circ}\text{S}$ - $0^{\circ}$ ,  $90^{\circ}$ - $110^{\circ}\text{E}$ ; Saji et al. 1999). Anomalies are defined as the deviation from the monthly climatology for the period from 2000 to 2014. A 5-month running mean filter and a 3-month

triangle filter are applied. Gray shades highlight anomalies that exceed one standard deviation in magnitude, indicating Indian Ocean Dipole events.

Fig. 2: Climatological zonal velocity (colors) and potential density (contours) at (a,c,e)  $0^{\circ}$ ,  $78^{\circ}\text{E}$  and (b,d,f)  $0^{\circ}$ ,  $80.5^{\circ}\text{E}$ . Results are for (a,b) ADCP observations and (c-f) ORA-S4 output. Mean seasonal cycles for observational velocity are calculated based on record length means at each location for the period from 2005 to 2013. For comparison, ORA-S4 velocity time series are sampled at the same time period and locations, and the mean seasonal cycles calculated from the resulting time series are shown in (c) and (d). Velocity climatologies shown in (e) and (f) are calculated using the full time series (2005-2013) of reanalysis output. Climatologies for potential density are calculated using the full time series for both observations and the reanalysis. A 61-day triangle filter is applied. Results are very similar for filters ranging between 41-days to 81-days. Contour intervals for potential density are  $1.0 \text{ kg m}^{-3}$ .

Fig. 3: Same as Fig.2, but for (a,c,e)  $0^{\circ}$ ,  $83^{\circ}\text{E}$  and (b,d,f)  $0^{\circ}$ ,  $90^{\circ}\text{E}$ .

Fig. 4: Longitude-time sections of mean seasonal cycles of zonal velocity for ADCP observations at (a) 10-m, (b) 80-m and (c) 120-m depths along the equator. Triangle marks illustrate the longitudes of ADCP moorings. Mean seasonal cycles are calculated based on record-length means. (d-f) Same as (a-c), respectively, but for ORA-S4 zonal velocity which is sampled with the same time history and locations as ADCP observations. (g-i) Same as (d-f), respectively, but calculated from the full time series (2005-2013) of the ORA-S4 reanalysis. The period for

the calculation of mean seasonal cycles is from 2005 to 2013. A 61-day triangle filter is applied. Results are very similar for filters ranging between 41-days to 81-days.

Fig. 5: Temporally averaged wavelet power for mean seasonal cycles of zonal velocity obtained from ADCP observations at (a) 78°, (b) 80.5°, (c) 83° and (d) 90°E on the equator. Mean seasonal cycles are calculated based on record length means for the period from 2005 to 2013. We have omitted to show power that is below the 95% confidence level. Dotted vertical line illustrates the period of 180 days. Horizontal lines show isopycnal depths averaged over the same period obtained from observed temperature and salinity. Contour intervals are  $1 \text{ kg m}^{-3}$ . (e-h) Same as (a-d), respectively, but for ORA-S4. Mean seasonal cycles for reanalysis velocity are calculated for the same period but using the full time series over 2005-2013.

Fig. 6: Zonal phase speed at the period of 180 days for mean seasonal cycles of zonal velocity obtained from ADCP observations on the equator. Phase speed between (a) 78° and 83°E and (b) 80.5° and 90°E. Positive and negative phase speed means eastward and westward propagation, respectively. Gray shade indicates that corresponding power is below the 95% confidence level. Solid lines show potential density at (a) 80.5°E and (b) 85°E on the equator obtained from observations. Contour intervals are  $1 \text{ kg m}^{-3}$ . Mean seasonal cycles for observed zonal velocity are calculated based on record length means for the period from 2005 to 2013, and those for potential density are calculated using the full time series for the same period.

768 Fig. 7: Same as Fig.6, but for ORA-S4.

769 Fig. 8: Zonal phase speed at the period of 180 days for mean seasonal cycles of zonal  
770 velocity along the equator obtained from ORA-S4 at (a) 10-m, (b) 80-m and (c)  
771 120-m depths. Zonal interval for phase speed calculation is  $10^\circ$ . Gray shade  
772 indicates that zonal phase estimates are unavailable, because the corresponding  
773 power is below the 95% confidence level. Positive/negative phase speed means  
774 eastward/westward propagation.

775 Fig. 9: Zonal phase speed at the 180-day period for zonal velocity obtained from ADCP  
776 observations. Phase speed is calculated using phase between (a-c)  $78^\circ$  and  $83^\circ\text{E}$   
777 and (d-f)  $80.5^\circ$  and  $90^\circ\text{E}$  on the equator. Phase speed at (a,d) 10-m, (b,e) 80-m and  
778 (c,f) 120-m depths is shown. Colors denote year. Positive/negative phase speed  
779 means eastward/westward propagation. We excluded the phase from the  
780 calculation if the corresponding power is below the 95% confidence level.

781 Fig. 10: (a) Climatological zonal wind stress along the equator for the period from 2005  
782 to 2013 obtained from the ECMWF reanalysis. A 61-day triangle filter is applied.  
783 (b) Corresponding zonal phase speed at the period of 180 days calculated using  
784 wavelet analysis. Positive/negative phase speed means eastward/westward  
785 propagation. Triangles indicate ADCP mooring locations. Note that we obtained  
786 similar propagation tendencies if we calculated mean seasonal cycles of zonal  
787 wind for the full time period of the ERA interim reanalysis (1989 to 2014).

788 Fig. 11: Monthly climatologies for zonal wind averaged over  $5^\circ\text{S}$  to  $5^\circ\text{N}$  obtained from  
789 the ECMWF reanalysis (colors) and outgoing longwave radiation (OLR) averaged

over 20°S to 20°N obtained from NOAA Interpolated OLR (contours; Liebmann and Smith 1996). Climatological seasonal cycles are repeated twice. OLR exceeding 250 W m<sup>-2</sup> was excluded from the meridional average, as OLR lower than this value indicates atmospheric deep convection (Motell and Weare, 1987). Climatologies are calculated for the period from 2005 to 2013 coincident with the observations.

Fig. 12: (a) Temporally averaged wavelet power at the period of 180 days for climatological zonal wind stress along the equator. The period for climatology is from 2005 to 2013. (b,c) Brunt-Väisälä frequency along the equator averaged over the period from 2005 to 2013. Solid lines show ray paths for (b) Kelvin waves and (c) the first meridional mode Rossby waves at the period of 180 days. Kelvin and Rossby rays are calculated based on the WKB approximation following McCreary (1984).

# Figures

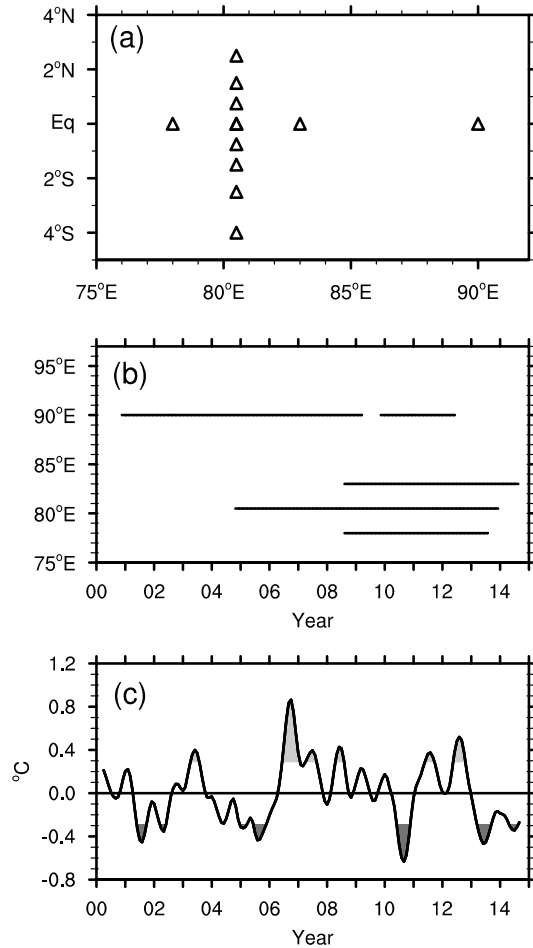
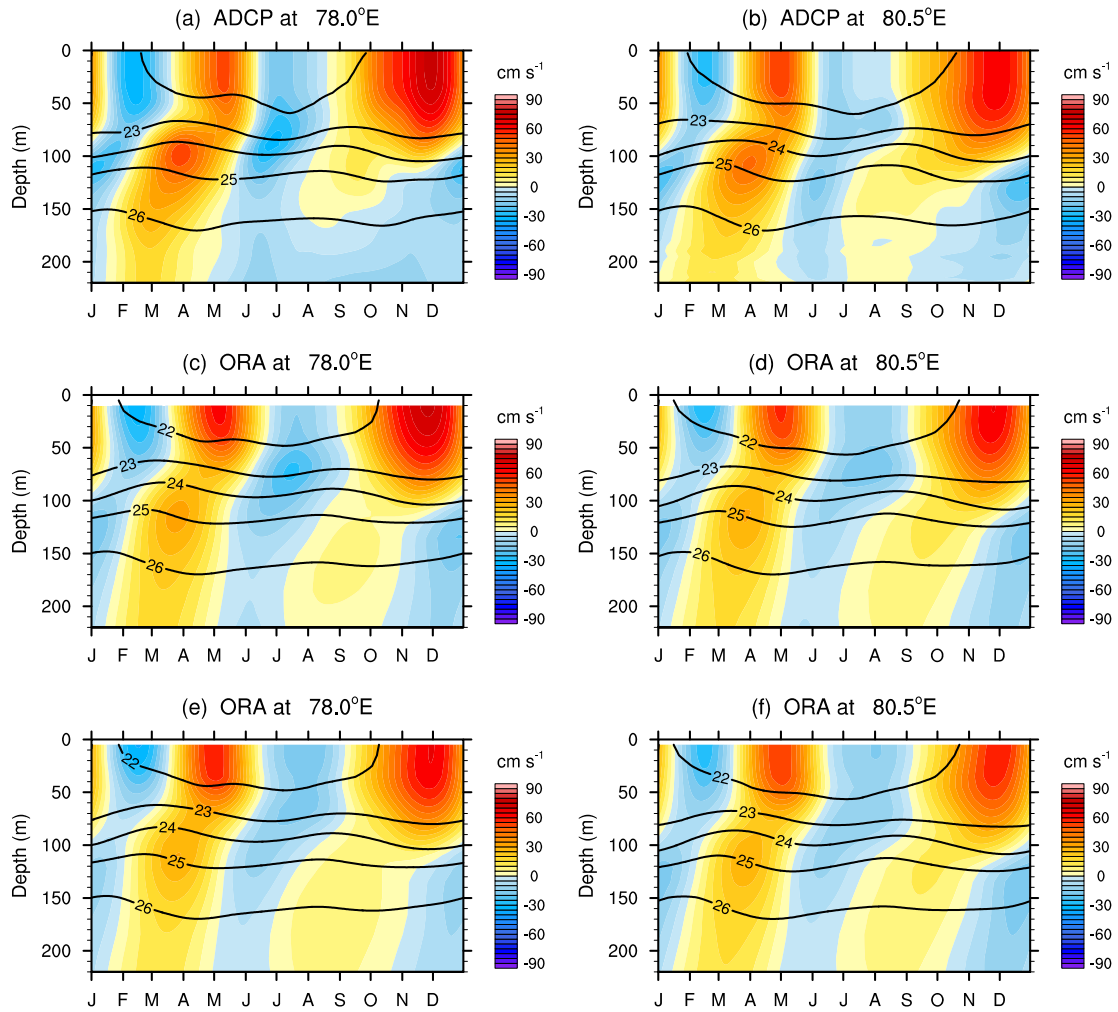


Fig. 1: (a) Locations of ADCP mooring sites (78°E, 80.5°E, 83°E and 90°E along the equator; 4°S, 2.5°S, 1.5°S, 0.75°S, 0°, 0.75°N, 1.5°N, and 2.5°N along 80.5°E). (b) Time history of ADCP sampling along the equator. The time series is from 9 August 2008 to 28 July 2013 at 78°E, from 27 October 2004 to 6 December 2013 at 80.5°E, from 8 August 2008 to 18 August 2014 at 83°E, and from 17 November 2000 to 5 June 2012 at 90°E. The data gap at 90°E is from 19 March 2009 to 10 November 2009. (c) The index to the Indian Ocean dipole calculated from monthly averages of sea surface temperature (SST) obtained from the National Oceanic and Atmospheric Administration (NOAA) Optimum Interpolation (OI) SST dataset Version 2 (Reynolds et al. 2002). The Dipole mode index is defined as the difference in SST anomalies between the

western Indian Ocean (10°S-10°N, 50°-70°E) and the eastern equatorial Indian Ocean (10°S-0°, 90°-110°E; Saji et al. 1999). Anomalies are defined as the deviation from the monthly climatology for the period from 2000 to 2014. A 5-month running mean filter and a 3-month triangle filter are applied. Gray shades highlight anomalies that exceed one standard deviation in magnitude, indicating Indian Ocean Dipole events.

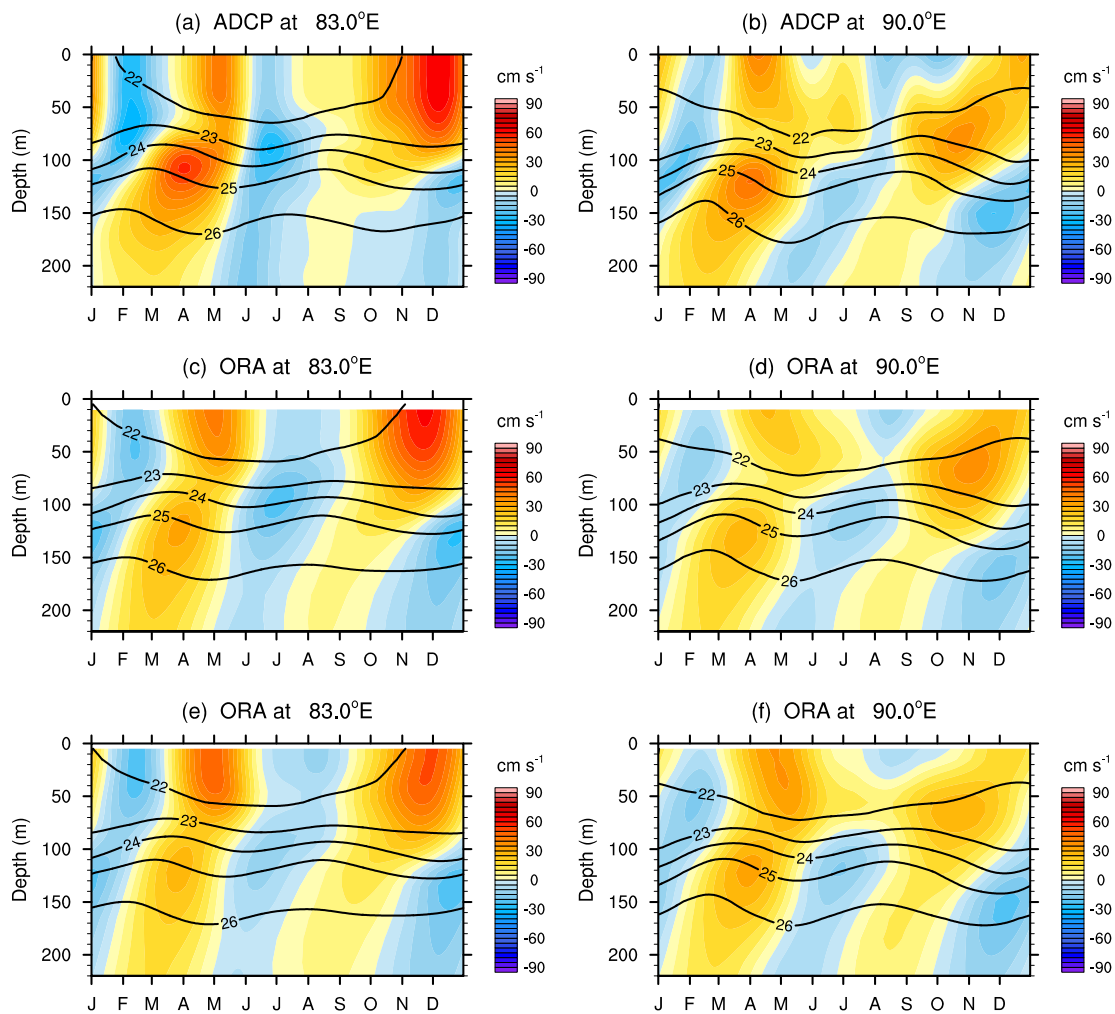


860

861

862 Fig. 2: Climatological zonal velocity (colors) and potential density (contours) at (a,c,e)  
 863 0°, 78°E and (b,d,f) 0°, 80.5°E. Results are for (a,b) ADCP observations and (c-f)  
 864 ORA-S4 output. Mean seasonal cycles for observational velocity are calculated based  
 865 on record length means at each location for the period from 2005 to 2013. For  
 866 comparison, ORA-S4 velocity time series are sampled at the same time period and  
 867 locations, and the mean seasonal cycles calculated from the resulting time series are  
 868 shown in (c) and (d). Velocity climatologies shown in (e) and (f) are calculated using  
 869 the full time series (2005-2013) of reanalysis output. Climatologies for potential density  
 870 are calculated using the full time series for both observations and the reanalysis. A  
 871 61-day triangle filter is applied. Results are very similar for filters ranging between  
 872 41-days to 81-days. Contour intervals for potential density are  $1.0 \text{ kg m}^{-3}$ .

873



874

875

876 Fig. 3: Same as Fig.2, but for (a,c,e) 0°, 83°E and (b,d,f) 0°, 90°E.

877

878

879

880

881

882

883

884

885

886

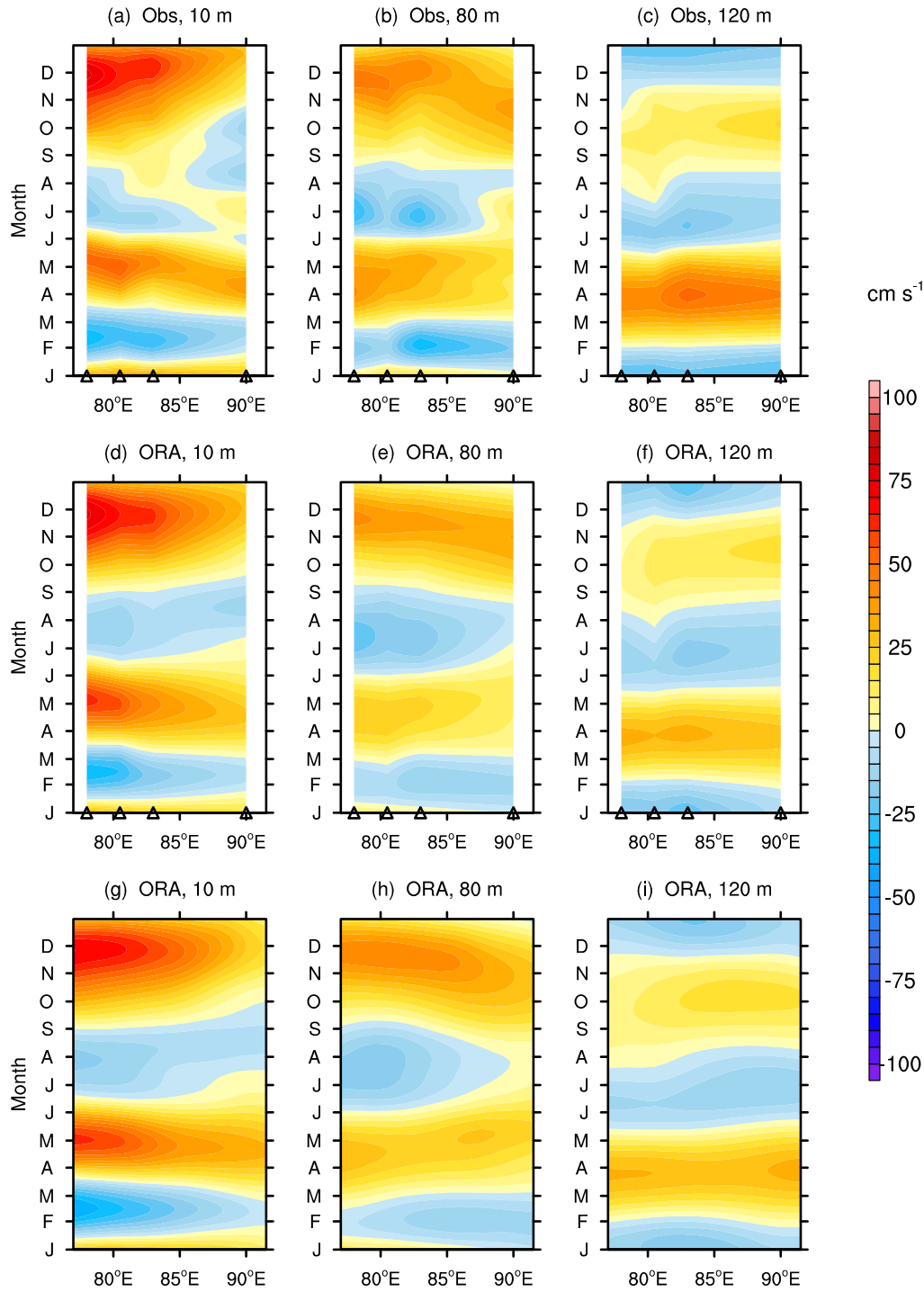
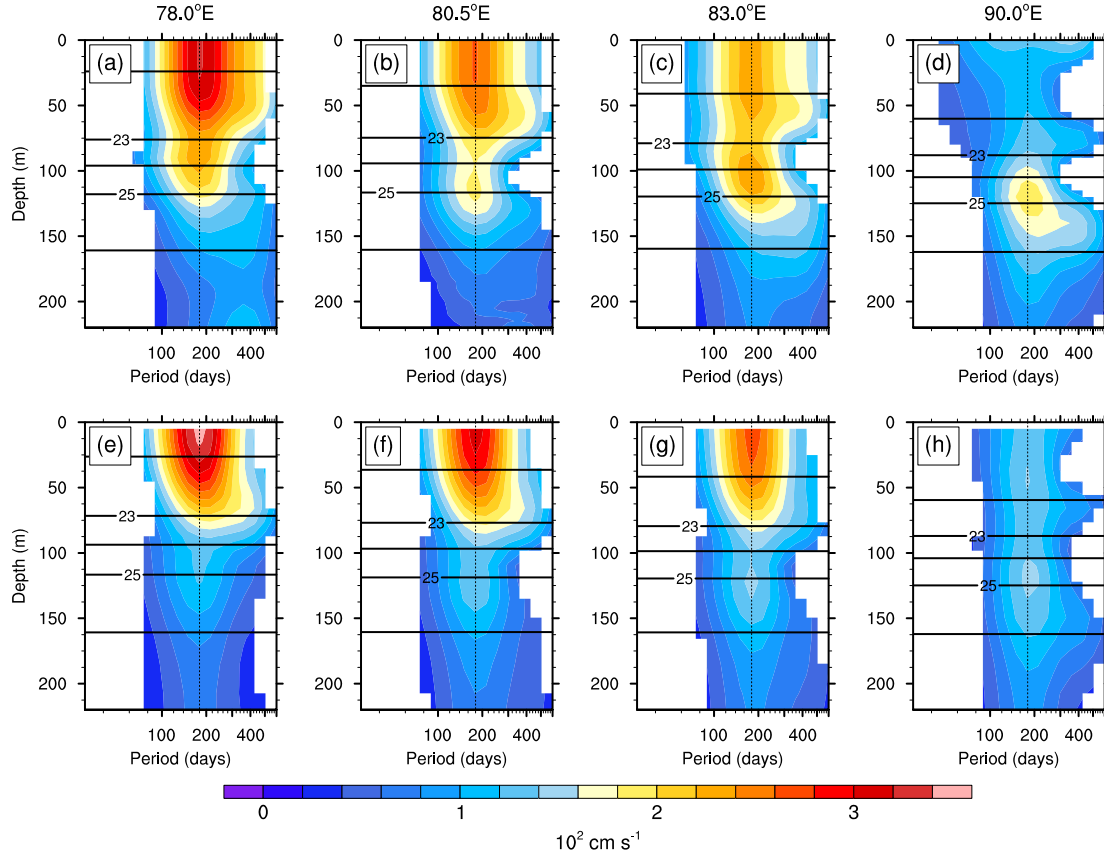


Fig. 4: Longitude-time sections of mean seasonal cycles of zonal velocity for ADCP observations at (a) 10-m, (b) 80-m and (c) 120-m depths along the equator. Triangle marks illustrate the longitudes of ADCP moorings. Mean seasonal cycles are calculated based on record-length means. (d-f) Same as (a-c), respectively, but for ORA-S4 zonal

velocity which is sampled with the same time history and locations as ADCP observations. (g-i) Same as (d-f), respectively, but calculated from the full time series (2005-2013) of the ORA-S4 reanalysis. The period for the calculation of mean seasonal cycles is from 2005 to 2013. A 61-day triangle filter is applied. Results are very similar for filters ranging between 41-days to 81-days.

926  
927



928  
929

930 Fig. 5: Temporally averaged wavelet power for mean seasonal cycles of zonal velocity  
931 obtained from ADCP observations at (a) 78°, (b) 80.5°, (c) 83° and (d) 90°E on the  
932 equator. Mean seasonal cycles are calculated based on record length means for the  
933 period from 2005 to 2013. We have omitted to show power that is below the 95%  
934 confidence level. Dotted vertical line illustrates the period of 180 days. Horizontal lines  
935 show isopycnal depths averaged over the same period obtained from observed  
936 temperature and salinity. Contour intervals are  $1 \text{ kg m}^{-3}$ . (e-h) Same as (a-d),  
937 respectively, but for ORA-S4. Mean seasonal cycles for reanalysis velocity are  
938 calculated for the same period but using the full time series over 2005-2013.

939  
940  
941  
942

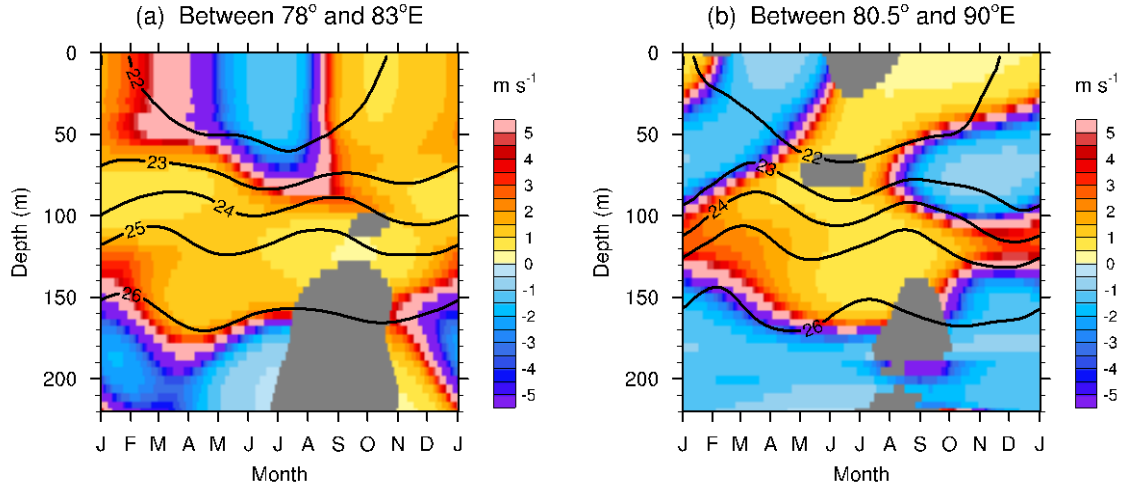


Fig. 6: Zonal phase speed at the period of 180 days for mean seasonal cycles of zonal velocity obtained from ADCP observations on the equator. Phase speed between (a) 78° and 83°E and (b) 80.5° and 90°E. Positive and negative phase speed means eastward and westward propagation, respectively. Gray shade indicates that corresponding power is below the 95% confidence level. Solid lines show potential density at (a) 80.5°E and (b) 85°E on the equator obtained from observations. Contour intervals are  $1 \text{ kg m}^{-3}$ . Mean seasonal cycles for observed zonal velocity are calculated based on record length means for the period from 2005 to 2013, and those for potential density are calculated using the full time series for the same period.

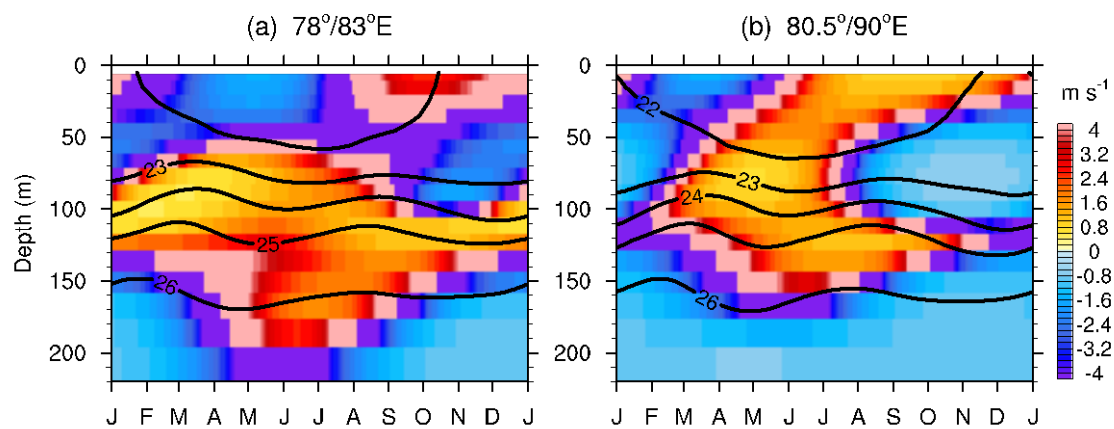


Fig. 7: Same as Fig.6, but for ORA-S4.

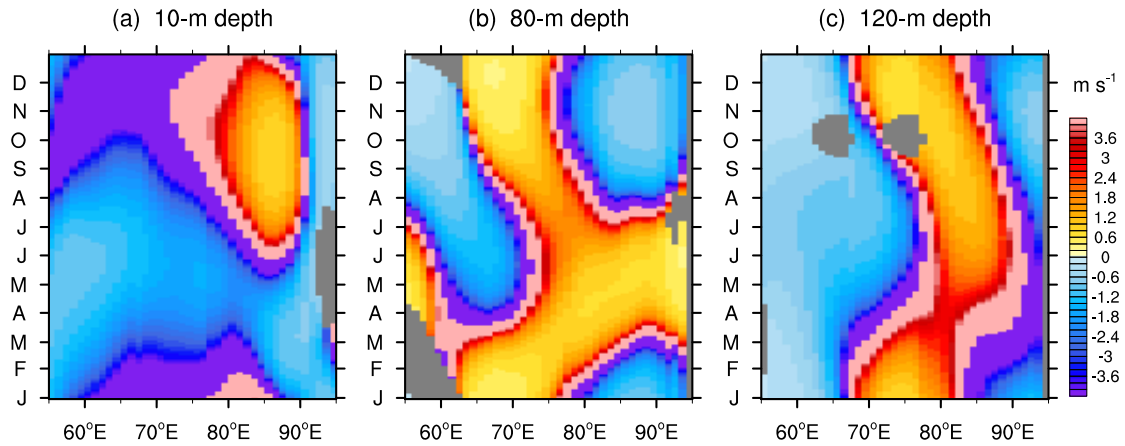
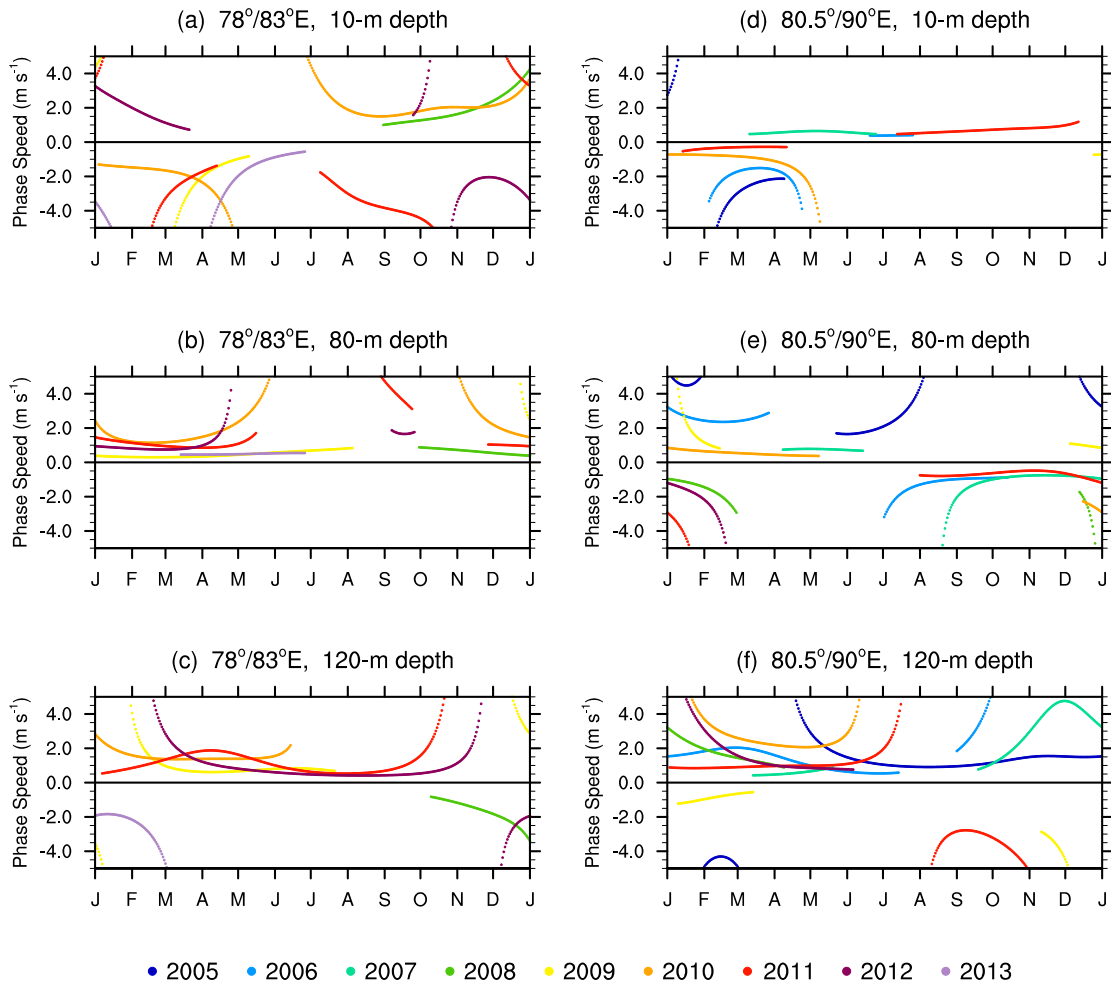


Fig. 8: Zonal phase speed at the period of 180 days for mean seasonal cycles of zonal velocity along the equator obtained from ORA-S4 at (a) 10-m, (b) 80-m and (c) 120-m depths. Zonal interval for phase speed calculation is  $10^\circ$ . Gray shade indicates that zonal phase estimates are unavailable, because the corresponding power is below the 95% confidence level. Positive/negative phase speed means eastward/westward propagation.

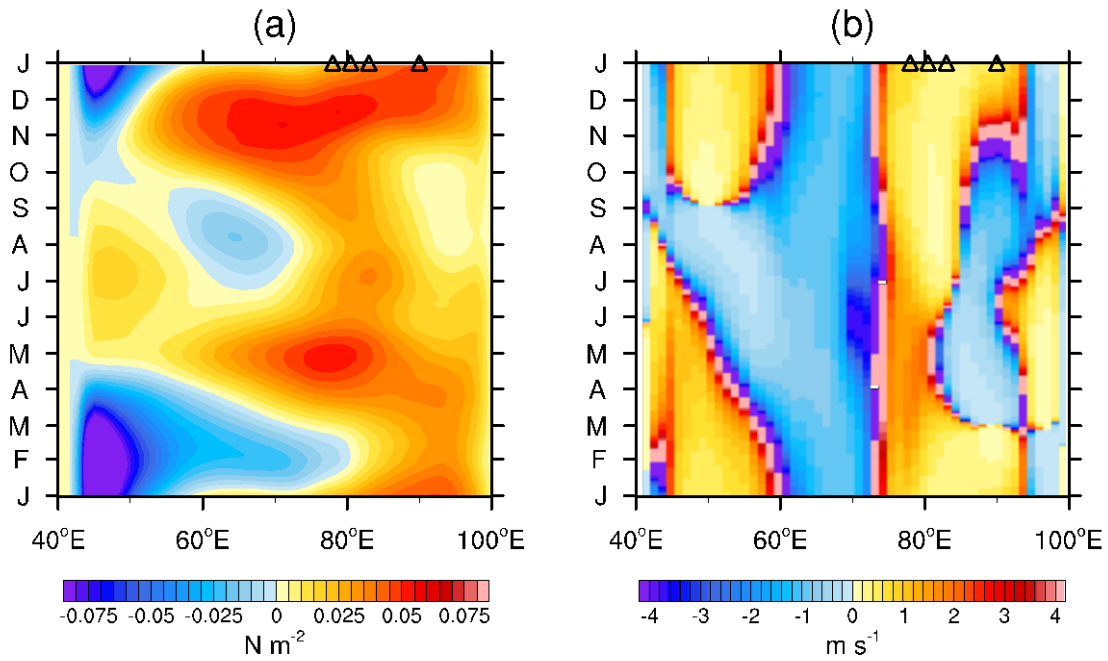
1017  
1018



1019  
1020  
1021  
1022  
1023  
1024  
1025  
1026  
1027  
1028  
1029  
1030  
1031

Fig. 9: Zonal phase speed at the 180-day period for zonal velocity obtained from ADCP observations. Phase speed is calculated using phase between (a-c) 78° and 83°E and (d-f) 80.5° and 90°E on the equator. Phase speed at (a,d) 10-m, (b,e) 80-m and (c,f) 120-m depths is shown. Colors denote year. Positive/negative phase speed means eastward/westward propagation. We excluded the phase from the calculation if the corresponding power is below the 95% confidence level.

1032  
1033



1034  
1035

1036 Fig. 10: (a) Climatological zonal wind stress along the equator for the period from 2005  
1037 to 2013 obtained from the ECMWF reanalysis. A 61-day triangle filter is applied. (b)  
1038 Corresponding zonal phase speed at the period of 180 days calculated using wavelet  
1039 analysis. Positive/negative phase speed means eastward/westward propagation.  
1040 Triangles indicate ADCP mooring locations. Note that we obtained similar propagation  
1041 tendencies if we calculated mean seasonal cycles of zonal wind for the full time period  
1042 of the ERA interim reanalysis (1989 to 2014).

1043  
1044  
1045  
1046  
1047  
1048  
1049  
1050

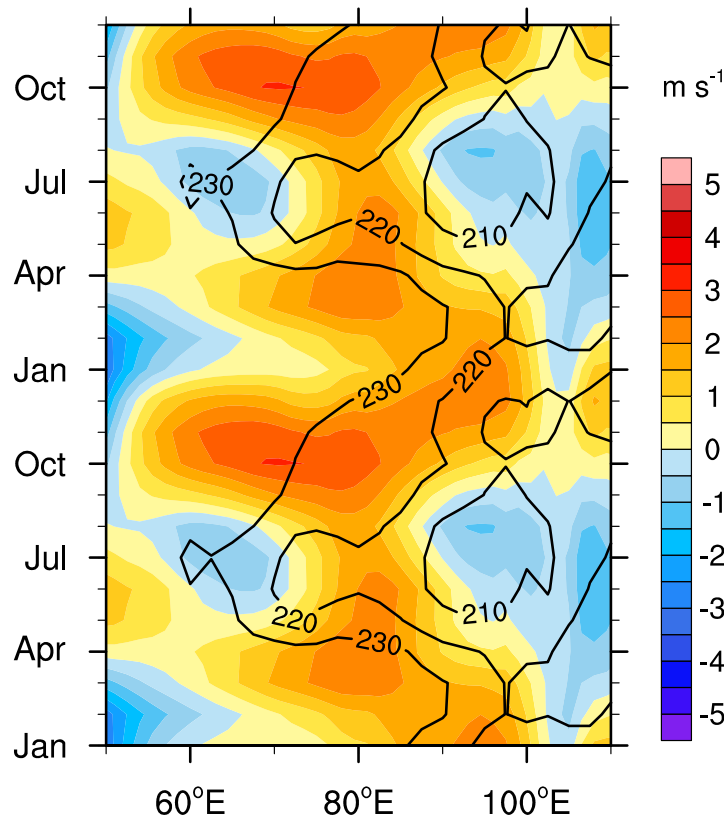


Fig. 11: Monthly climatologies for zonal wind averaged over 5°S to 5°N obtained from the ECMWF reanalysis (colors) and outgoing longwave radiation (OLR) averaged over 20°S to 20°N obtained from NOAA Interpolated OLR (contours; Liebmann and Smith 1996). Climatological seasonal cycles are repeated twice. OLR exceeding 250 W m<sup>-2</sup> was excluded from the meridional average, as OLR lower than this value indicates atmospheric deep convection (Motell and Weare, 1987). Climatologies are calculated for the period from 2005 to 2013 coincident with the observations.

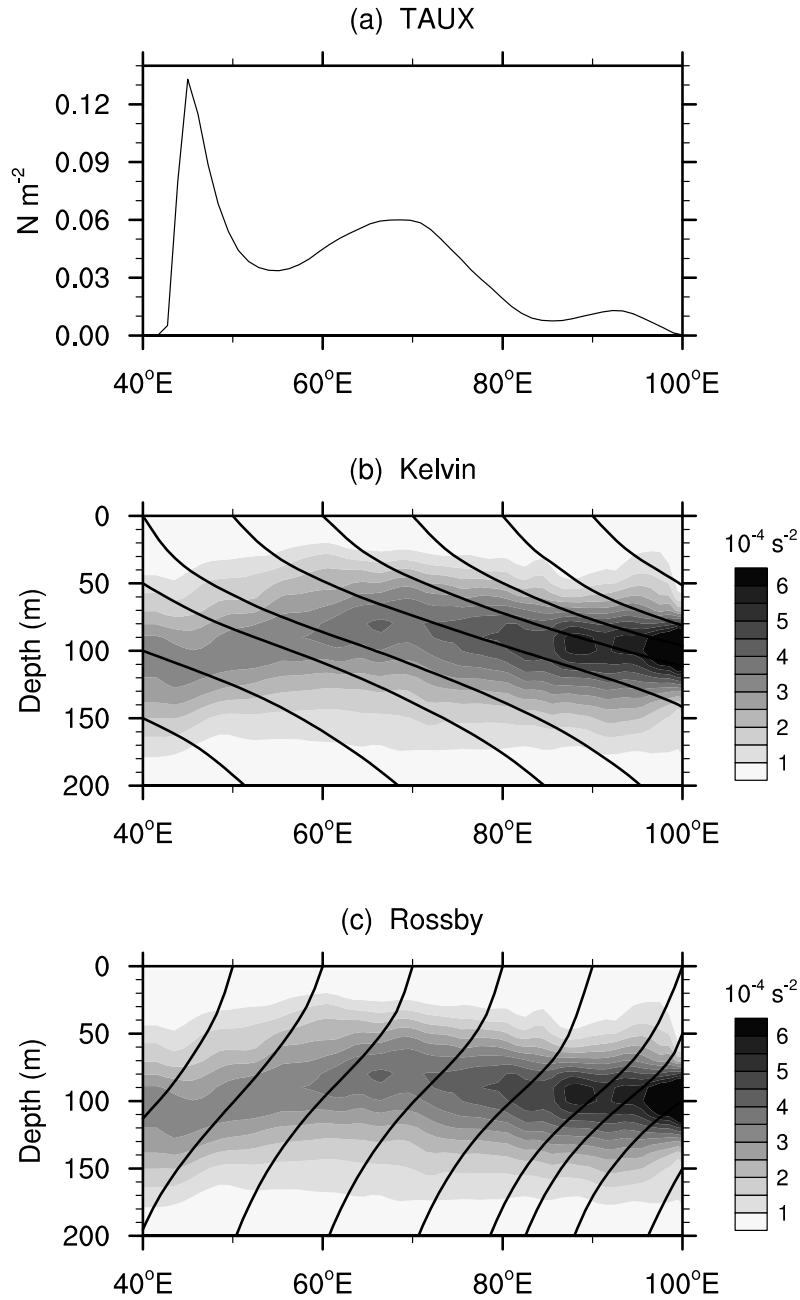
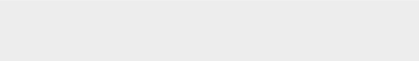


Fig. 12: (a) Temporally averaged wavelet power at the period of 180 days for climatological zonal wind stress along the equator. The period for climatology is from 2005 to 2013. (b,c) Brunt-Väisälä frequency along the equator averaged over the period from 2005 to 2013. Solid lines show ray paths for (b) Kelvin waves and (c) the first meridional mode Rossby waves at the period of 180 days. Kelvin and Rossby rays are calculated based on the WKB approximation following McCreary (1984).




Click here to access/download  
**Non-Rendered Figure**  
Figure1.pdf





Click here to access/download  
**Non-Rendered Figure**  
Figure2.pdf



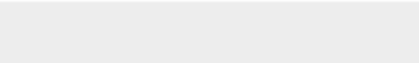

Click here to access/download  
**Non-Rendered Figure**  
Figure3.pdf




Click here to access/download  
**Non-Rendered Figure**  
Figure4.pdf

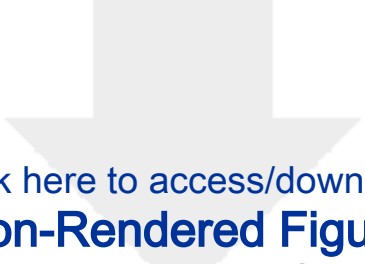


Click here to access/download  
**Non-Rendered Figure**  
Figure5.pdf

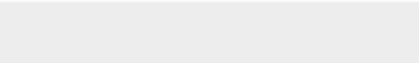



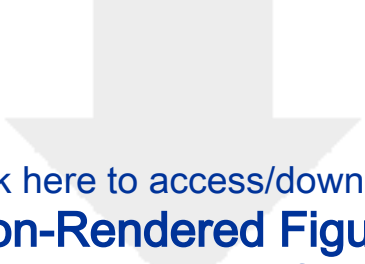


Click here to access/download  
**Non-Rendered Figure**  
Figure6.pdf

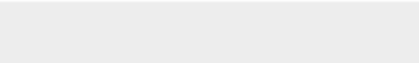



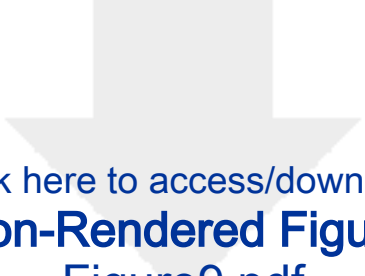
Click here to access/download  
**Non-Rendered Figure**  
Figure7.pdf



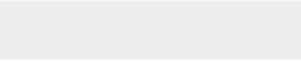


Click here to access/download  
**Non-Rendered Figure**  
Figure8.pdf





Click here to access/download  
**Non-Rendered Figure**  
Figure9.pdf





Click here to access/download  
**Non-Rendered Figure**  
Figure10.pdf





Click here to access/download  
**Non-Rendered Figure**  
Figure11.pdf





Click here to access/download  
**Non-Rendered Figure**  
Figure12.pdf

